Chemical Engineering Journal 525 (2025) 170464

Contents lists available at ScienceDirect

Chemical Engineering Journal

journal homepage: www.elsevier.com/locate/cej

Unleashing instant on-site naked-eye detection by a portable NIR-SPR platform with organic upconversion

Li-Chen Su [a,b,*], Xin-Hui Wang [a], Chun-Jen Shih [a], Zhi-Hao Huang [c], Ying-Feng Chang [d,e], Chen-Kai Chang [f], Chi-Yun Wang [g,h], Yu-Ching Huang [a,c,f,i,*], Shun-Wei Liu [a,j,*]

[a] Organic Electronics Research Center, Ming Chi University of Technology, New Taipei City, 24301, Taiwan
[b] General Education Center, Ming Chi University of Technology, New Taipei City, 24301, Taiwan
[c] Department of Chemical and Materials Engineering, Chang Gung University, Taoyuan, 33302, Taiwan
[d] Artificial Intelligence Research Center, Chang Gung University, Taoyuan, 333323, Taiwan
[e] Department of Gastroenterology and Hepatology, New Taipei Municipal Tu Cheng Hospital (Built and Operated by Chang Gung Medical Foundation), New Taipei, 236017, Taiwan
[f] Department of Materials Engineering, Ming Chi University of Technology, New Taipei City, 24301, Taiwan
[g] International Ph.D. Program in Innovative Technology of Biomedical Engineering and Medical Devices, Ming Chi University of Technology, New Taipei City, 24301, Taiwan
[h] Research Center for Intelligent Medical Devices, Ming Chi University of Technology, New Taipei City, 24301, Taiwan
[i] Biochemical Technology R&D Center, Ming Chi University of Technology, New Taipei City, 24301, Taiwan
[j] Department of Electronic Engineering, Ming Chih University of Technology, New Taipei City 24301, Taiwan

ARTICLE INFO

Keywords:
NIR SPR
Organic upconversion
Infrared imaging
One-pot assay

ABSTRACT

Surface plasmon resonance (SPR) sensing offers label-free, real-time biomolecular detection, but conventional SPR systems remain confined to laboratory settings due to their size, cost, and need for trained operators. Smartphone-based SPR platforms mitigate these constraints via built-in cameras, yet visible-light SPR produces broad resonance dips and is unable to access the sharper, higher-figure-of-merit (FOM) signals available in the near-infrared (NIR) due to IR-cut filters. Here, we introduce a portable NIR-SPR biosensor that integrates an organic upconversion device (OUD) to convert NIR resonance signals into bright green emission—entirely without infrared photodiode arrays or complex optics. The OUD comprises a PTB7-Th:COTIC-4F bulk heterojunction charge-generation layer and a ZnO:PDINO-passivated anode interface, achieving a high upconversion quantum efficiency of 18.12 %. When integrated into our NIR-SPR platform, the OUD not only preserves the sharper resonance dips and elevated FOM of NIR interrogation but, through a reference line, produces a simple yes/no ("fringe/no-fringe") visual output. We demonstrate one-pot detection of African swine fever (ASF)–associated miRNAs (ssc-miR-122 and ssc-miR-199a-5p) at ≥5 nM in both buffer and diluted pig serum within 10 min, with no nucleic-acid amplification steps. This naked-eye platform—optionally smartphone-capturable—can be readily extended to other infectious-disease biomarkers. To our knowledge, it is the first portable SPR system enabling direct miRNA detection by simple visual readout—an unexplored approach in the literature with significant innovation potential for decentralized diagnostics.

1. Introduction

Surface plasmon resonance (SPR) sensing enables label-free and real-time monitoring of biomolecular interactions by measuring refractive-index changes at a metal-dielectric interface [1–3]. Although laboratory-based SPR systems offer high sensitivity and have been widely adopted from environmental toxin screening to clinical analysis, their bulk, cost, and need for specialized operators render them impractical for on-site applications in agriculture, livestock disease surveillance, and environmental monitoring. [4–8]. To overcome these barriers, there is growing interest in portable SPR platforms with rapid, intuitive readouts.

Smartphone-based SPR platforms have emerged as cost-effective alternatives for visible-light SPR readout, leveraging built-in cameras

* Corresponding authors at: Organic Electronics Research Center, Ming Chi University of Technology, New Taipei City, 24301, Taiwan.
E-mail addresses: sulichen@mail.mcut.edu.tw (L.-C. Su), huangyc@mail.mcut.edu.tw (Y.-C. Huang), swliu@mail.mcut.edu.tw (S.-W. Liu).

https://doi.org/10.1016/j.cej.2025.170464
Received 6 March 2025; Received in revised form 19 October 2025; Accepted 3 November 2025
Available online 4 November 2025

to capture reflectance changes and track resonance shifts [7,9–12]. However, visible-light SPR yields relatively broad resonance features that limit contrast and angle-shift resolution. One strategy to address this is to operate SPR sensors in the near-infrared (NIR) region, where the longer wavelength produces inherently sharper resonance dips and a higher figure of merit (FOM) [13–17], thereby reducing uncertainty in resonance angle determination and improving signal contrast. Unfortunately, most smartphone cameras employ IR-cut filters to block infrared light and ensure accurate visible-light image reproduction, but this also attenuates NIR signals and prevents direct NIR-SPR readout [18]. To date, no platform has integrated this enhanced NIR detection performance into a truly portable, user-intuitive visual readout.

To overcome this limitation, we developed a portable NIR-SPR platform that integrates an organic upconversion device (OUD) to enable direct, naked-eye observation of resonance shifts. The OUD converts NIR signals into visible light, eliminating the need for infrared cameras or photodiode arrays and providing a simple, intuitive visual readout. Structurally, the OUD consists of a photodiode-LED stack that allows real-time infrared-to-visible conversion without the need for costly pixelated sensors or readout circuits [19–22]. Recent advances in upconversion efficiency and material design have further enhanced the brightness and responsiveness of these devices [23–25], making them suitable for practical field applications.

In this study, we employ a bulk heterojunction of PTB7-Th:COTIC-4F as the NIR-responsive charge-generation layer (CGL) and a ZnO:PDINO-passivated anode interface [26], which together enhance electron extraction and luminance under NIR excitation to achieve an upconversion quantum efficiency of 18.12 %—the highest reported efficiency without external gain mechanisms. When incorporated into our NIR-SPR platform, the OUD enables a distinct “fringe/no-fringe” visual output guided by a reference line. This intuitive yes/no readout allows users to visually interpret the results without complex instrumentation, supporting rapid decision-making in field diagnostics using either the naked eye or standard smartphone cameras.

To validate the system, we tested its ability to detect African swine fever (ASF)-associated miRNA biomarkers, demonstrating successful detection in both buffer solutions and simulated real-world samples. Currently, ASF diagnosis relies on qPCR, a highly sensitive method that, while accurate, requires thermal cycling, specialized laboratory infrastructure, and trained personnel, making it impractical for independent use by farm personnel. Recently, miRNA detection has been explored as a promising method for ASF diagnosis [27–30]. Unlike qPCR, certain miRNA detection strategies can bypass nucleic acid amplification [31], enabling simplified workflows compatible with on-site diagnostics. However, no commercially available rapid assays currently exist for detecting ASF-associated miRNA biomarkers. Our platform addresses this unmet need by offering a lightweight, portable system with a one-step amplification-free assay format and a rapid 10-min detection time. The direct visual readout eliminates the need for complex equipment or trained operators, empowering farm personnel to conduct reliable, timely diagnostics. This approach not only fills a critical gap in ASF surveillance but also provides a broadly applicable framework for decentralized miRNA-based diagnostics. With its modular design and simplified components, the platform is well-suited for scalable deployment across a variety of point-of-need biosensing applications, particularly in resource-limited settings.

2. Materials and methods

2.1. Materials and OUDs fabrication

PTB7-Th, COTIC-4F, and PDINO were purchased from 1-Material Inc. BCzPh, Ir(ppy)$_2$(acac), and LiF were purchased from Lumtec. Shine Materials provided CN-T2T. Zinc acetate was obtained from Alfa Aesar. 2-Methoxylethanol, ethanolamine, chlorobenzene (CB), ortho-xylene (o-xylene), 1-chloronaphthalene (CN), and PEIE were received from Sigma-Aldrich. All reagents and solvents were used as received without further purification. The device was fabricated on indium tin oxide (ITO) substrates provided by Lumtec, which were cleaned with deionized water, acetone, and isopropanol beforehand. A charge extraction layer of sol-gel ZnO was developed on the substrate with a mixture of 0.25 M PDINO or PEIE, followed by post-annealing at 180 °C for 30 min. PEIE, an amine-functionalized polymer, is widely used to passivate oxygen vacancies in ZnO; however, its thermal and chemical compatibility with non-fullerene acceptors (NFAs) can be limited due to amine-carbonyl interactions. Besides, it requires precise control over the PEIE equivalent owing to its insulating nature, which challenges the introduction of applying OUD for large-area imaging applications. In our previous study, we found that PDINO—a perylene diimide derivative known for its favorable energy-level alignment and chemical stability—is an alternative solution to suppress oxygen defects in the ZnO layer, along with improved interface stability [26]. For this reason, PDINO was selected as an alternative interlayer modifier to promote electron extraction compared to PEIE in this study.

The substrates were then transferred to the N_2-filled glovebox. The PTB7-Th: COTIC-4F solution (20 mg/mL in ortho-xylene with 0.5 vol% CN) was spin-coated at 3000 rpm for 30 s, developing a 70 nm photoactive layer for NIR detection. After that, the device was finalized by transferring to a thermal evaporator, stacking light-emitting diode of BCzPh (40 nm)/ BCzPh:CN-T2T:Ir(ppy)2(acac) (1:1:10 %, 30 nm)/ CN-T2T (50 nm)/ LiF (1 nm)/ aluminum (120 nm). The thickness of each layer was characterized with ellipsometry measurements (Raditech SE-950). The device area was 0.04 cm^2, defined by the overlapping ITO and aluminum pattern. The complete devices were transferred to the N_2-filled glovebox (O_2 < 0.1 ppm; H_2O < 0.1 ppm) for encapsulation. A glass-to-glass sealing process was performed using a UV-curable epoxy resin (Everwide Chemical Corporation Limited EXC345) to prevent exposure to ambient air during performance characterization.

2.2. OUDs characterization

The current density-luminance-voltage characteristics of the device were recorded with LQ-100R (Enlitech), coupled with a 940 nm laser (CNI laser). An extra mask covering the device area defined the active region (2.27 mm^2). The EQE spectra were characterized with the QE-R3011 system (Enlitech). The infrared-to-visible upconversion quantum efficiency was calculated according to the equation of

$$\eta_{p-p}\,(\%) = \frac{\#photon_{VIS}}{\#photon_{NIR}} = \int \frac{\lambda_{up} I_{up}(\lambda)}{hc} d\lambda \Big/ \frac{\lambda_{inc} P_{inc}}{hc}$$

All measurements followed the protocol developed in the previous literature to avoid overestimation [25].

2.3. Design principles and operational setup

The OUD-based NIR-SPR sensor operates using an angular interrogation setup, as shown in Fig. 1a, which illustrates the configuration of the system’s optical components. A 980 nm diode laser serves as the light source. The laser beam is directed through a polarization beam splitter (PBS) with an extinction ratio of 1000:1, effectively filtering out the s-polarized component and allowing only the p-polarized wave to propagate. This selective polarization ensures optimal coupling with the SPR device, maximizing SPR excitation and enhancing contrast. The polarized light then passes through a 30 mm focal length lens, forming a convergent beam that strikes the sensor surface at an optimal range of incident angles. After reflecting off the SPR device, the light is redirected by a flat mirror to increase the optical path length, thereby magnifying the image. Finally, the beam illuminates the OUD, which is specifically designed to convert NIR light into visible green light. A green emission zone appears on the OUD, within which a distinct dark line represents the SPR dip. This dip shifts its position in response to changes in the

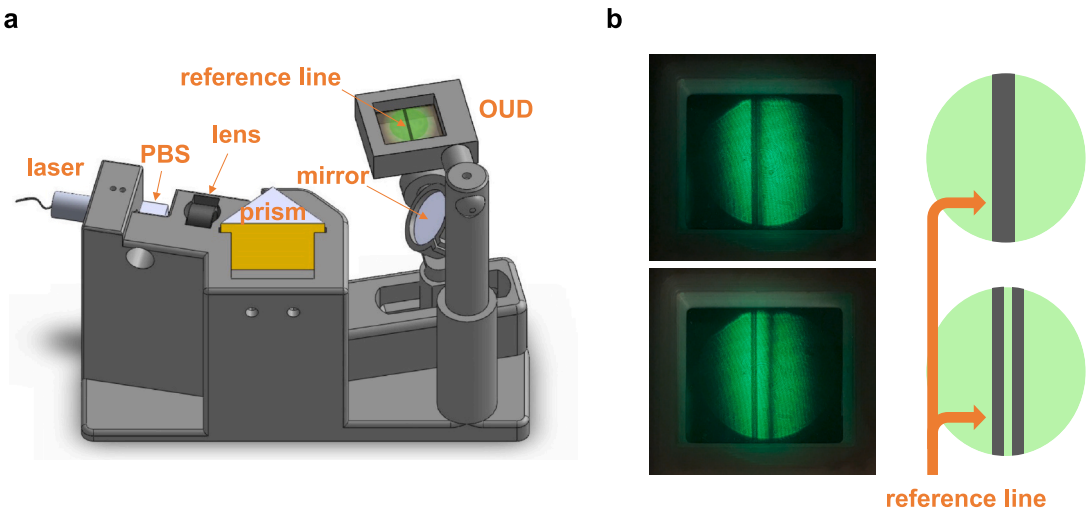

Fig. 1. Schematic illustration and operational setup of the OUD-based NIR-SPR sensor. a) Schematic of the angular interrogation setup, detailing the configuration of optical components including the NIR light source, PBS, lens, mirror, and the specially designed OUD that converts NIR light to visible green light. b) Illustration of the detection setup featuring a movable reference line positioned adjacent to the left boundary of the SPR dip, allowing straightforward identification of SPR signal shifts.

analyte's refractive index (RI), enabling easy, naked-eye observation of the sensor's response.

To facilitate direct visualization of SPR signal shifts, we implemented a movable "reference line" positioned immediately adjacent to the left boundary of the SPR dip (dark line), as shown in Fig. 1b. During each assay, the analyte introduction increases the effective RI near the chip surface, causing the SPR dip to shift toward larger angles (observed as a rightward movement in our system). A bright-green fringe appears between the reference line and the shifted SPR dip, with its width directly proportional to analyte concentration. To ensure that the reference line remains in a reproducible position relative to the SPR dip across all experiments, we mounted a thin PET mask printed with the reference line on a micrometer-driven translation stage (5 μm accuracy, 10 μm per main division). Prior to each measurement, the micrometer was adjusted—while viewing the live smartphone feed—until the reference line lay immediately adjacent to the SPR dip. A calibration showed that advancing the micrometer stage by 5 mm produces a 151-pixel shift in the image—equivalent to ≈ 33 μm per pixel. Over five independent alignments, the stage readings showed a standard deviation of 11 μm (≈ 0.3 pixel), confirming sub-pixel reproducibility. Consequently, any observed fringe shift ≥1 pixel reflects true SPR-dip movement rather than positioning error. This simple yet robust scheme—combining a calibrated, movable reference line with high-contrast OUD illumination—allows rapid naked-eye observation of SPR shifts without the need for complex optics or image processing. The resulting benchtop instrument has a total weight of only 650 g and dimensions of approximately 190 × 100 × 170 mm (Fig. S1), thus maximizing portability and on-site applicability.

2.4. Biomolecule detection

2.4.1. Probe immobilization

To demonstrate the practical potential of our system, we selected two ASF-associated miRNA biomarkers in pigs—ssc-miR-122 and ssc-miR-199a-5p—as targets. [27–30]. Streptavidin-immobilized sensor chips (Cytiva) were used for robust attachment of biotinylated DNA molecules. A 2 μM solution of each biotinylated DNA probe (complementary to the target miRNA) in running buffer (10 mM Tris-HCl, pH 7.4, 15 mM $MgCl_2$) was injected into the SPR flow-cell for 20 min, enabling stable probe anchoring.

Prior to on-chip assays, the probe immobilization conditions were optimized on a commercial Biacore SPR system. The surface probe density was adjusted by co-injecting biotinylated DNA with free biotin at various ratios (1:0, 1:0.25, 1:0.5). As shown in Fig. S2, the immobilization and functional responses increased with probe fraction, with the 1:0 surface providing the highest signal without compromising hybridization efficiency. Therefore, the 1:0 ratio was selected as the optimal probe-density condition for subsequent assays.

2.4.2. Assay in running buffer

A solution of target miRNAs and S9.6 antibody in running buffer was injected into the SPR flow cell and incubated with the immobilized probes for 10 min to allow DNA–RNA hybridization and subsequent antibody binding. After incubation, unbound components were removed by washing with running buffer, ensuring that only specifically bound probe–miRNA–antibody complexes remained.

2.4.3. Assay in pig serum matrix

To evaluate performance in complex samples, pig serum (Sigma Aldrich, P9783) was spiked with synthetic miRNAs and S9.6 antibody, then supplemented with 10 % (*v*/v) of Cytiva NSB reducer stock (10 mg/mL carboxymethyl dextran in 0.15 M NaCl, 0.02 % NaN_3) as a surface anti-fouling reagent [32,33]. The resulting sample was introduced into the SPR flow cell and incubated for 10 min, during which the NSB reducer competitively occupies non-specific adsorption sites while specific probe-miRNA-antibody complexes form. After incubation, unbound serum components, excess NSB reducer, and free antibody were removed by washing with running buffer, ensuring that only specifically bound complexes remained on the sensor surface.

These procedures, including both the probe immobilization and the interaction with the miRNA-antibody mixture, were recorded using a smartphone (iPhone 12 mini), and the corresponding videos are provided in the Supporting information.

2.5. Gel electrophoresis

The hybridization of DNA probes with miRNA was assessed using 6 % native polyacrylamide gel electrophoresis (PAGE) in 0.5× TBE buffer (45 mM Tris base, 45 mM boric acid, 1 mM EDTA, pH 8.3). The electrophoresis was carried out at 120 V for the first 5 min, followed by 80 V for an additional 45 min. The gel was subsequently stained with SYBR™ Gold Nucleic Acid Gel Stain. Additionally, S9.6 antibody was used to bind to DNA/RNA hybrids, further validating the interaction for SPR signal amplification. Visualization of the gels was performed using a gel

imaging system (Major Science UVCI-01) and CCD camera (PCO sCMOS camera).

2.6. Fringe-width analysis from smartphone images

While our OUD-SPR platform is engineered for rapid, naked-eye readout, we also implemented a fully automated pipeline to extract quantitative fringe-width measurements from smartphone-captured videos. This Python/OpenCV workflow converts raw video frames into pixel-based data in four sequential stages:

2.6.1. Frame extraction & slicing

Videos recorded with an iPhone 12 mini serve as raw input. For image analysis, the original 30 fps video was subsampled at 1 fps (one frame every 30 frames). Each extracted frame (1920 × 1080) was then divided into 20 horizontal slices by averaging every 100 vertical pixels, yielding data of shape (20, 1080), which we convert to grayscale using Python's OpenCV module.

2.6.2. Smoothing

We apply a moving-average filter to the 1D intensity profile of each horizontal slice.

2.6.3. Peak-based region selection and FWHM calculation

For each smoothed profile, the two highest peaks are detected automatically and used as boundaries to isolate the region between them; we then compute its full width at half maximum (FWHM).

2.6.4. Fringe-width determination

The 20 FWHM values are sorted in descending order, and the average of the middle eight values is taken as the width of the bright-green fringe for that frame.

3. Results and discussion

3.1. Performance characterization of NIR OUDs

As shown in Fig. 2a, we develop an OUD device structure that generates visible luminance upon NIR excitation, following our previous demonstration that brings an invisible NIR signal to sight [25]. However, instead of the ZnO charge-extraction layer (CEL) modified with conventional PEIE, we incorporate the same molar amount of PDINO in the sol-gel ZnO layer in this work. Compared to the device built upon the conventional ZnO-PEIE composite, the OUD built upon hybrid ZnO-PDINO CEL shows a two times more significant photocurrent density (J_{ph}) of 2.24 mA cm^{-2} at 6.0 V under a NIR power density of 1.0 mW cm^{-2} (Fig. 2b). This signifies the beneficial character of the PDINO for promoting charge extraction from the PTB7-Th: COTIC-4F CGL, which aligns with the results observed in our previous study that the electron mobility of the PEIE-based photodetectors is about one order of magnitude lower than that of the PDINO-based photodetectors, regardless of the PEIE ratio. As a result, an upconversion visible luminance of 475.39 cd m^{-2} is captured at 6.0 V from the OUD that comprises the ZnO-PDINO CEL under the same NIR excitation intensity (Fig. 2c), where limited luminance below 1.0 cd m^{-2} is detected under dark even at the bias voltage of 6.0 V. We further explore the charge generation performance of the device with the external quantum efficiency (EQE) measurement in Fig. 2d. The higher EQE performance of the OUD developed on the ZnO-PDINO CEL validates the superior charge extraction ability of the proposed composite layer, which can be ascribed to the semiconducting nature of the PDINO. However, a comparable specific detectivity in the NIR spectrum is derived in Fig. 2e. This can be attributed to the dominant noise current contributed by the light-emitting diodes in the OUD structure, as discovered in our recent study [24]. On the effect of the improved charge extraction, the infrared-to-visible upconversion quantum efficiency of the OUD is increased from 15.04 % to 18.12 % after replacing PEIE with PDINO in the ZnO CEL (Fig. 2f), one of the highest values in the literature harnessing the non-

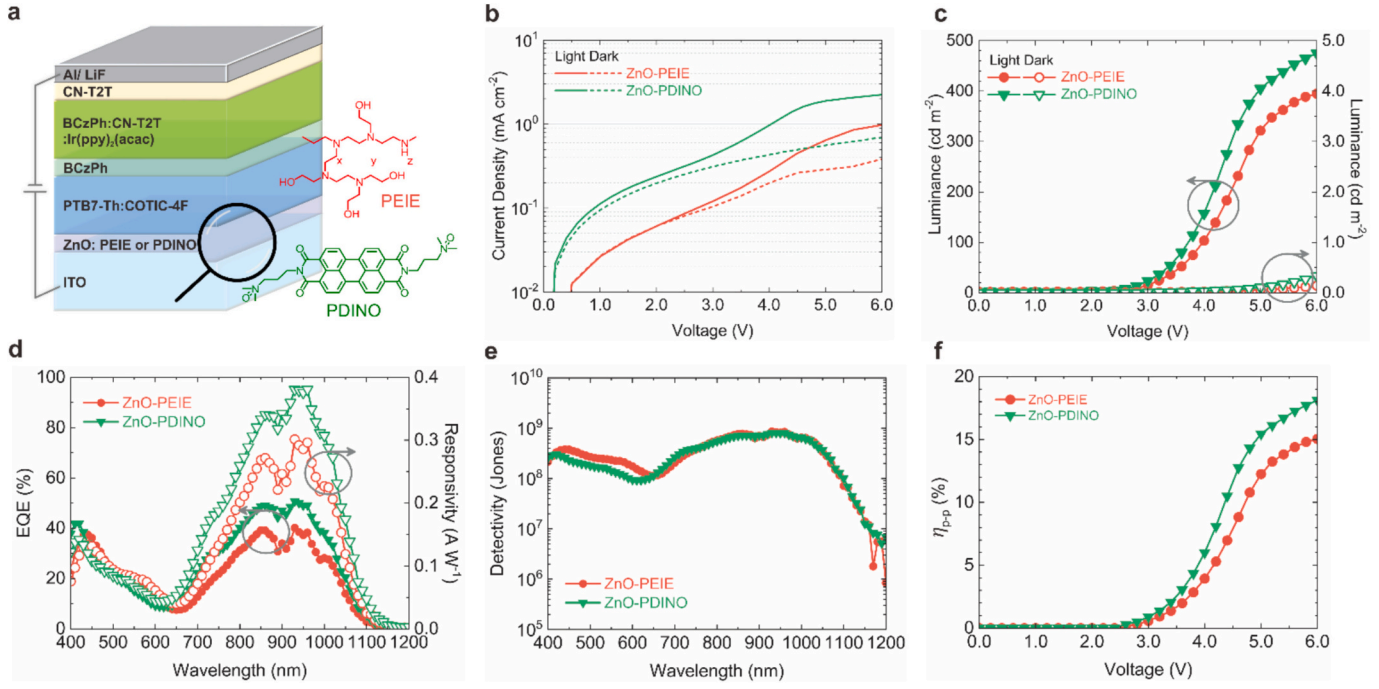

Fig. 2. Device performance of the NIR OUD. a) The OUD device structure developed upon sol-gel ZnO modified with PEIE or PDINO. b) Current density-voltage characteristics of the device under 1.0 mW cm^{-2} of the 940 nm laser. c) Upconverted visible luminance of the device under the same infrared stimulus. d) EQE and responsivity spectra of the device at 6.0 V. e) The specific detectivity spectra of the device biased at 6.0 V. f) The infrared-to-visible upconversion quantum efficiency of the device under the infrared power density of 1.0 mW cm^{-2}.

fullerene CGL.

As described in Section 2.1, the devices were hermetically encapsulated before testing. Luminance stability was then monitored under continuous NIR illumination at 1.0 mW cm^{-2}, room temperature and 50 % relative humidity (RH), showing no measurable degradation over 48 h of operation (Fig. S3a). Under accelerated aging conditions (10 mW cm^{-2}), the upconversion luminance declined by approximately 10 % after 1458 min (24 h) of continuous operation, demonstrating solid stability even at elevated irradiance. Additionally, thermal aging at 70 °C and 50 % RH resulted in a 50 % reduction in luminance after 2130 min (35 h) of continuous operation, reflecting the upper bounds of current material endurance under extreme conditions that far exceed those encountered in field applications.

To further evaluate the operational stability of the complete OUD-SPR assembly, we conducted a 30 h continuous-operation test under an irradiance of ≈ 0.29 mW cm^{-2} (4.5 mW total power), corresponding to the actual operating condition used in the sensing experiments. The bright-green fringe after the SPR dip shift remained clearly visible before and after the aging test (Fig. S3b), with a drift in fringe width below 3 %, indicating negligible influence of device degradation on sensing performance. In addition, functional tolerance was assessed using neutral-density (ND) filters to simulate luminance decay of aged OUDs (Fig. S3c). The bright-green fringe remained clearly visible up to 0.6 OD (25 % transmittance) and still discernible at 1.0 OD (10 % transmittance), demonstrating robust visual readability even when the OUD output was significantly attenuated. These findings confirm the long-term operational reliability of the OUD-based NIR-SPR system under realistic environmental conditions.

3.2. Detection performance of the OUD-based NIR-SPR biosensor with naked-eye detection

In this section, we evaluate the detection performance of the proposed OUD-based NIR-SPR biosensor with naked-eye detection. Using Macleod simulation software, we first compare the SPR angular spectrum at 635, 780, and 980 nm (Fig. 3a). Relative to the commonly used red light at 635 nm, the 980 nm spectrum exhibits a much narrower FWHM (∼ 6 ×) and a modestly lower RI sensitivity (∼ 1.4 ×), resulting in a substantially higher FOM^{+} (∼ 5 ×). Since FOM^{+} incorporates both the depth and width of the resonance feature, it provides a more comprehensive metric for evaluating sensor performance [34].

At 780 nm, all three metrics fall between 635 and 980 nm: the FWHM is ∼ 2× narrower than 635 nm, the sensitivity is ∼ 1.3× lower, and the $FOMs^{+}$ is ∼ 2.3× higher than 635 nm. These wavelength-dependent trends indicate that moving toward longer wavelengths yields narrower and deeper resonance dips and higher $FOMs^{+}$, thereby yielding a more contrasted SPR curve and enhancing naked-eye discernibility in our OUD-based system.

To highlight the advantages of using an NIR light source combined with a specially designed OUD for naked-eye SPR observation, we conducted a comparative analysis between the visual SPR dips observed in a red-light SPR system and our NIR system. In the following experiments, all observed SPR signal images, as perceived by the naked eye, were captured using the smartphone and presented. The SPR dip (dark line) in the red-light system is broader and exhibits less defined edges, leading to lower contrast compared to the NIR system, as shown in Fig. 3b. This finding aligns with theoretical simulations, which indicate that SPR excitation at shorter wavelengths results in a greater FWHM. While shorter wavelengths theoretically offer higher sensitivity, the practical benefits of a narrower, more contrasted SPR curve at longer wavelengths—like those in the NIR system—lead to a higher FOM^{+}. Consequently, the NIR system, in combination with the specially designed OUD, proves to be more effective for developing naked-eye SPR observation platforms. This is further demonstrated in Fig. 3c, where the SPR dip shifts observed visually are significantly clearer and more easily distinguishable in the NIR system than in the red-light system under identical RI variations.

To systematically evaluate the performance of the OUD-based NIR-SPR system, we conducted experiments using glycerol-water solutions at concentrations of 0 %, 0.125 %, 0.25 %, 0.5 %, 1 %, and 1.5 %, carefully monitoring the corresponding SPR dip shifts. As shown in Fig. 3d, no SPR dip shift was observed at 0 % glycerol concentration, and consequently, no bright-green fringe appeared. However, as the glycerol concentration increased, the SPR dip shift became more pronounced, resulting in a widening of the bright-green fringe between the two dark lines. At the lowest concentration of 0.125 %, a faint bright-green fringe was still visible, corresponding to a RI change of 1.41×10^{-4} RIU—closely matching the theoretical detection limit of 1.20×10^{-4} RIU, which was calculated based on the system's optical configuration and the naked-eye resolution limit of 100 μm. To further quantify the physical performance of the system, we conducted triplicate measurements at each refractive-index increment (each glycerol-water concentration; raw data shown in Fig. S4). The mean width of the bright-green fringe (in pixels) at each Δn was plotted and subjected to linear regression (Fig. 3e), yielding a calibration slope of $S = 2.99 \times 10^{4}$ px/RIU ($R^2 = 0.992$). The standard deviation of the blank measurement (Δn = 0) across three replicates was σ(blank) = 0.124 px. Consequently, the refractive-index resolution is calculated to be 4.1×10^{-6} RIU, which surpasses those reported for smartphone-based SPR systems [10–12].

3.3. Feasibility of the biosensing strategy

The operational principle of the miRNA assay is illustrated in Fig. 4a. To verify the hybridization of DNA probes with miRNA and to assess the binding interactions of the S9.6 antibody with DNA-RNA hybrid structures, the probes and miRNA sequences were incubated with or without the S9.6 antibody, followed by analysis using 6 % native PAGE. As shown in Fig. 4b, both DNA probes demonstrated strong hybridization with their target miRNAs, as evidenced by the appearance of specific bands in lane 3 of each gel and the disappearance of individual probe and miRNA bands, indicating the successful formation of duplex structures. This confirms the specific interaction between the DNA probes and miRNAs.

To further evaluate the binding of the S9.6 antibody with DNA-RNA hybrids, an Electrophoretic Mobility Shift Assay (EMSA) was performed. In lane 3 of each gel, a specific band corresponding to the formation of DNA-miRNA duplex. In lane 6, where the S9.6 antibody was introduced, the band shifted to a higher molecular weight position, indicating strong binding of S9.6 to the DNA-miRNA hybrid. In contrast, lanes 4 (DNA probe with S9.6) and 5 (miRNA with S9.6) showed no shift in band position compared to lanes without the antibody, confirming that S9.6 specifically binds to DNA-RNA hybrids and not to single-stranded nucleic acids. These results demonstrate that the S9.6 antibody selectively and robustly binds to DNA-miRNA duplexes, highlighting its potential as an SPR signal amplification component in the biosensing strategy.

3.4. Performance of target microRNA detection

Our developed portable naked-eye SPR system offers exceptional convenience, making it ideal for on-site applications in environments such as farms, livestock facilities, and environmental monitoring sites. To demonstrate the practical application potential of our system, we selected miRNA biomarkers associated with ASF in pigs as the target analytes for this study. Given the low molecular weight of miRNAs (approximately 7 kDa), it was necessary to employ an SPR signal amplification technique to enhance sensitivity and improve detection limits. In this study, we selected the S9.6 antibody as our signal amplifier due to its ease of control and operation. The S9.6 antibody specifically recognizes DNA/RNA hybrids and does not cross-react with single-stranded DNA or RNA, DNA/DNA, and RNA/RNA hybrids [35–37]. Furthermore, we utilized a one-pot approach, where the signal amplifier

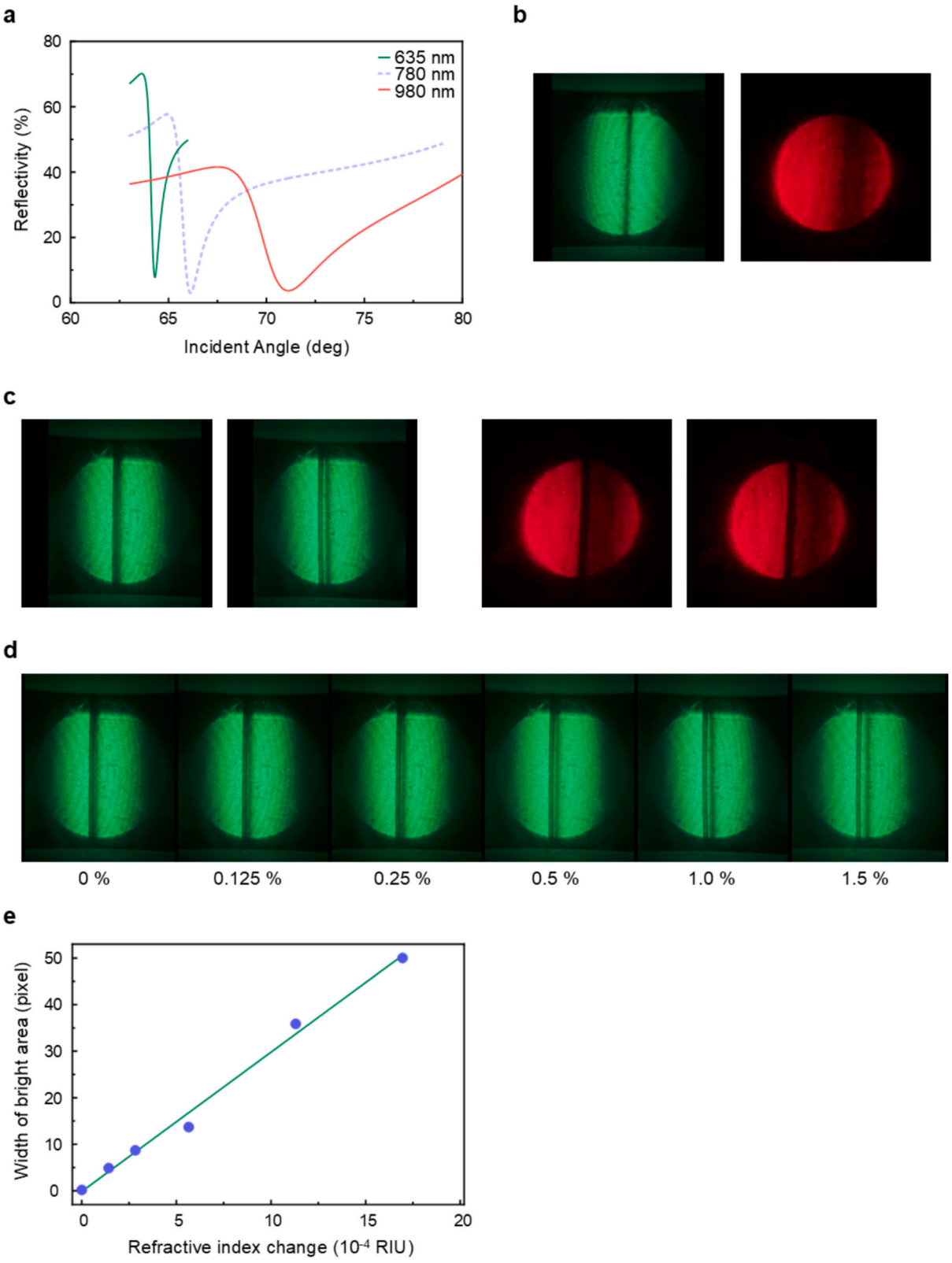

Fig. 3. Comparative analysis and evaluation of the OUD-based NIR-SPR biosensor. a) Simulated SPR angular reflectivity spectra at 635 nm, 780 nm, and 980 nm, obtained using Macleod software with water as the analyte medium ($n = 1.33$) and an incident angle sweep from 63° to 80°. The longer wavelengths exhibit sharper and deeper resonance features, leading to higher FOMs^{+} and highlighting the wavelength-dependent trend. b) Visual comparison of SPR dips in red-light and NIR SPR systems, illustrating sharper dips in the NIR system. c) Naked-eye observation of SPR dip shifts in NIR and red-light systems under the same RI variations. d) NIR SPR dip shifts observed in glycerol-water solutions with varying concentrations, highlighting the appearance and widening of bright-green fringes. e) Analysis of the relationship between the width of the bright-green fringes and RI changes. Data are shown as mean ± SD from three repeated experiments, and error bars are smaller than the symbol size.

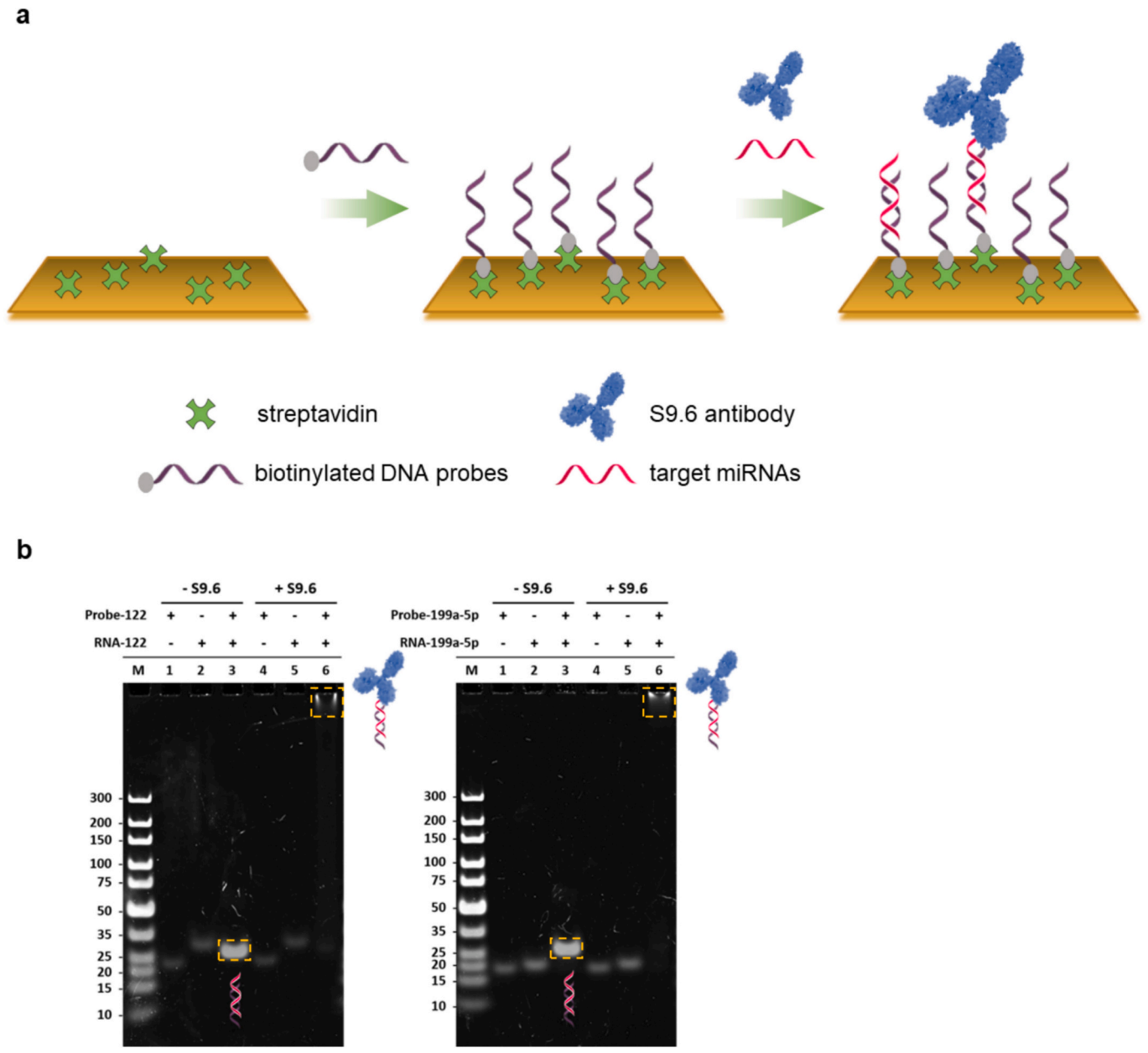

Fig. 4. Schematic and experimental validation of the biosensing strategy. a) Schematic illustration of the SPR biosensing strategy. b) Native PAGE results confirming the binding interactions in the biosensing strategy. Lanes 1: DNA probe; Lanes 2: miRNA; Lanes 3: DNA probe and miRNA hybrid; Lanes 4: DNA probe and S9.6 antibody; Lanes 5: miRNA and S9.6 antibody; Lanes 6: DNA probe, miRNA, and S9.6 antibody.

(S9.6 antibody) and the target miRNAs were mixed and directly injected into the system to interact with the DNA probes. This method is both convenient and straightforward, effectively reducing the complexity of the experimental procedure and shortening the reaction time, making it particularly suitable for portable on-site detection systems.

Fig. 5a presents the naked-eye patterns observed after a 10-min reaction period at various analyte concentrations. It is clear that for analyte concentrations above 5 nM, a shift in the SPR dip occurs, resulting in the appearance of a visible bright-green fringe between the dark lines. As the analyte concentration increases (5 nM, 10 nM, 20 nM, 40 nM), the shift in the SPR dip becomes more pronounced, leading to a progressively wider bright-green fringe. In contrast, for the blank sample (without targets), no bright-green fringe is observed in its naked-eye pattern due to no shift in the SPR dip. Furthermore, the relationship between the width of the bright-green fringe and analyte concentration was analyzed, as illustrated in Fig. 5b. This correlation supports the visual observations and confirms that our system is capable of detecting miRNAs at concentrations as low as 5 nM in buffer solution.

To further assess the applicability of our system in real-world settings, we conducted experiments using pig serum spiked with target miRNAs as a mimic of real samples to evaluate the system's performance in detecting miRNA within a biologically relevant matrix. To determine the optimal dilution factor that balances matrix complexity with signal clarity and reproducibility, SPR measurements were performed in triplicate on blank pig serum samples diluted 10-fold and 20-fold, using our standard washing protocol. As shown in Fig. S5, 10-fold diluted serum caused a persistent baseline drift in the SPR signal after washing, accompanies by a faint bright-green fringe, indicating non-specific adsorption of serum matrix that interferes with signal interpretation. In contrast, 20-fold diluted serum exhibited full baseline restoration and complete fringe disappearance, demonstrating that this level of dilution is sufficient to suppress matrix effects while maintaining biological

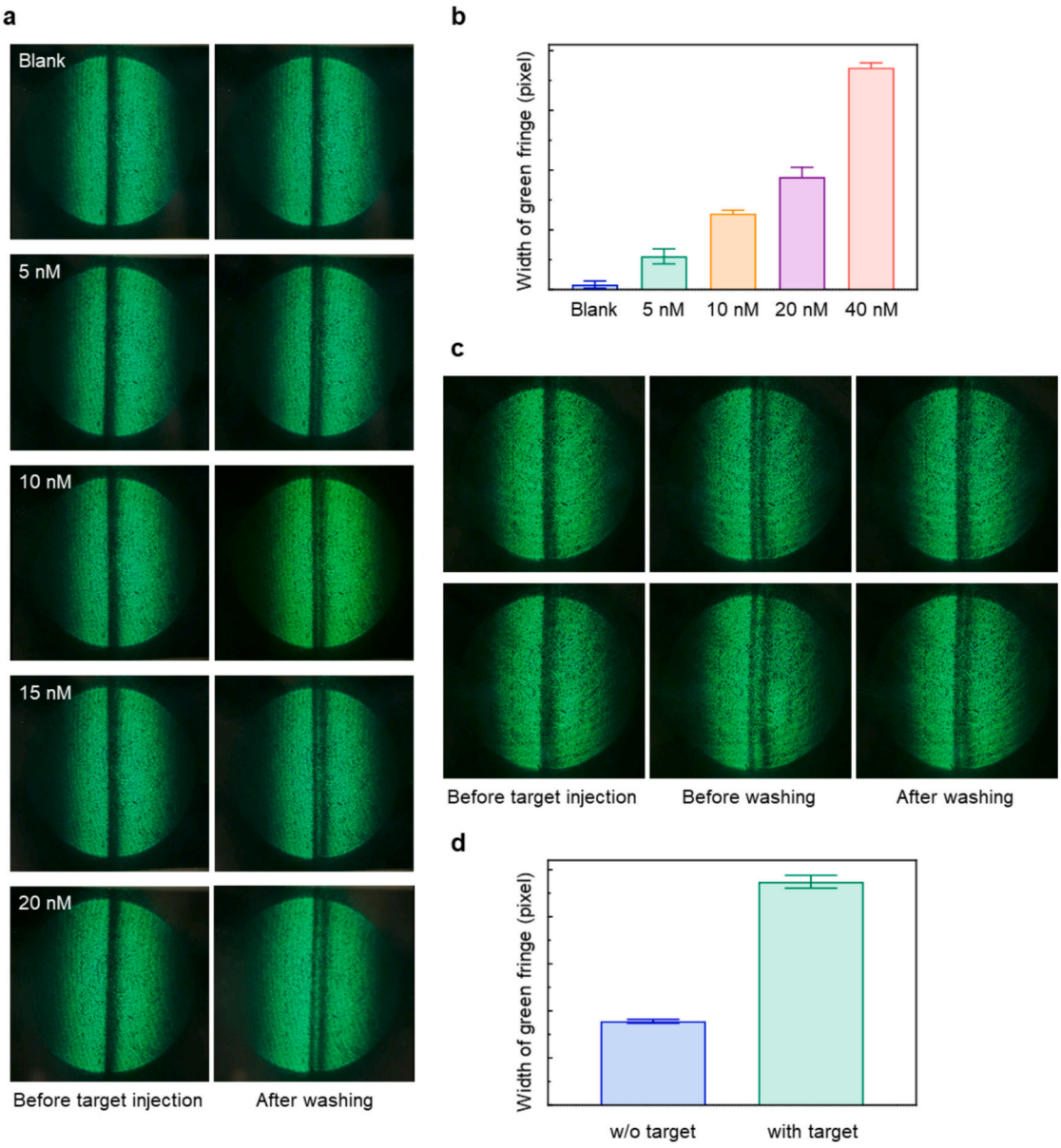

Fig. 5. Naked-eye detection of ASF-associated miRNAs using the portable OUD-based NIR-SPR system. a) Naked-eye patterns at various analyte concentrations (5 nM, 10 nM, 20 nM, 40 nM) and a blank sample. For each concentration, the left images show the patterns before the 10-min reaction, and the right images show the patterns after the reaction, highlighting the shift in SPR dip. b) Analysis of the relationship between the width of the bright-green fringe and analyte concentration, supporting the visual observations shown in (a). c) Detection of miRNAs in pig serum samples spiked without (upper panel) and with (lower panel) the target miRNAs. The left panel shows patterns before the reaction; the middle panel shows SPR dip shifts due to matrix effects; the right panel shows the patterns after washing. d) Analysis of the bright-green fringe's width in miRNA-spiked and control samples, demonstrating the system's capability to detect miRNA in complex biological matrices like pig serum. Error bars in (b) and (d) represent mean ± SD from 20 horizontal slices per frame.

complexity. Consequently, we adopted a 20-fold dilution protocol throughout all pig serum assays to ensure clear, unambiguous visual detection of analyte-induced SPR shifts in complex biological matrices. Following this protocol, pig serum samples were spiked with 5 nM of target miRNAs for detection. After a 10-min reaction period, we observed a shift in the SPR dip in both the miRNA-spiked and control samples (Fig. 5c, middle), likely due to matrix effects on the chip surface. Following a washing step, only the samples containing miRNA exhibited a visible bright-green fringe between the dark lines in the naked-eye pattern (Fig. 5c, right), while the control samples showed no such signal, as the non-specific matrix components were effectively washed away. Further analysis of the bright-green fringe's width (Fig. 5d) confirmed that in the samples spiked with 5 nM miRNA, the green fringe was significantly wider than in the control samples. These findings from both visual observation and width analysis demonstrate the feasibility of our system for detecting ASF-associated miRNAs in complex biological matrices like pig serum, reinforcing its potential for practical on-site diagnostic applications. Videos demonstrating the miRNA detection process are provided in the Supporting information, illustrating the experimental procedure and observations in detail.

Finally, to demonstrate assay specificity and exclude cross-reactivity, we evaluated the system using three abundant, disease-irrelevant miRNAs derived from pig spleen: ssc-miR-145-5p, ssc-miR-125b, and ssc-miR-143-3p [29,38]. In 20-fold diluted pig serum, we compared: (1) a non-target miRNA pool containing 10 nM each of the three irrelevant miRNAs and (2) a mixed sample comprising 5 nM ASF-specific miRNA plus the same non-target miRNA pool. Only the mixed sample produced a clear bright-green fringe, whereas the non-target miRNA pool alone

yielded no visible signal (Fig. S6). These results imply that our platform responds exclusively to ASF-associated miRNAs and rules out false positives due to cross-reactivity. To further benchmark our platform against the diagnostic gold standard, we performed quantitative real-time PCR (qPCR) on the same sets of samples: unspiked serum, non-target miRNA pool, and mixed samples containing both ASF-specific miRNAs (spiked at 0.5 nM and 40 nM) together with the non-target miRNA pool. As shown in Fig. S7, the unspiked serum (blank) and non-target miRNA pool produced high and equivalent Cq values, whereas samples containing both ASF-specific miRNAs (spiked at 0.5 nM and 40 nM) together with the non-target miRNA pool exhibited a pronounced, concentration-dependent reduction in Cq, consistent with our SPR observations. This strong agreement between OUD-SPR and qPCR confirms that our platform delivers reliable detection of ASF-associated miRNAs and verifies that the target sequences remain intact under our sample preparation conditions.

Table 1 presents a comparison of several recently developed naked-eye miRNA detection methods with our OUD-based NIR-SPR biosensor. While these methods achieve detection limits in the sub-nM to pM range, they primarily rely on nucleic acid amplification strategies, such as strand displacement amplification (SDA) [39], catalytic hairpin assembly (CHA) [40], rolling circle amplification (RCA) [41], and DNA walker circuits [42], as well as signal enhancement strategies, including nanozyme-mediated CRISPR/Cas12a assays [39]. While these approaches enable high sensitivity, their complexity and extended assay times (typically 1.5 to 3 h) make them less suited for on-site applications. Smartphone-based SPR platforms, valued for their portability and streamlined operation in on-site diagnostics, have to date been applied only to protein assays and have not yet been demonstrated for miRNA detection [7,11,12]. In contrast, our OUD-based NIR-SPR biosensor is the first portable SPR system enabling direct miRNA detection by simple visual readout—an unexplored approach with significant innovation potential for decentralized diagnostics. Amplification-free and requiring no complex instrumentation, our platform delivers real-time, naked-eye miRNA readout within 10 min, making it ideally suited for field-based disease surveillance in resource-limited settings.

4. Conclusions

In this study, we successfully developed a portable, naked-eye detection system by integrating an optimized OUD with high upconversion efficiency into a NIR SPR sensor. This system offers several critical advantages for practical biosensing applications. First, the use of OUDs provides a cost-effective and efficient approach to infrared signal visualization, eliminating the need for complex and expensive readout circuits. The absence of electronic components for signal processing also minimizes power consumption, making the system particularly suitable for battery-powered, field-deployable platforms. The optimized OUD, with an impressive upconversion quantum efficiency of 18.12 %, enhances the clarity of naked-eye detection by producing sharp contrast and distinct green light. This visual benefit, combined with the NIR SPR system's larger FOM^{+}, results in a more defined and contrasted SPR curve compared to conventional red-light systems. Consequently, the SPR dip shift generates a pronounced green fringe between the reference line and the SPR dip, allowing for straightforward, accurate interpretation of results without the need for sophisticated analytical tools. Additionally, the incorporation of antibodies that selectively bind to DNA/RNA hybrids directly into the assay enables a one-pot detection format with no nucleic-acid amplification steps. This not only amplifies the SPR signal but also simplifies the workflow, minimizes contamination risk, and shortens the total assay time to just 10 min. We demonstrate successful on-site detection of ASF-associated miRNA biomarkers in complex serum matrices, with a simple "fringe/no-fringe" readout that any untrained operator can interpret intuitively. This work extends SPR beyond the laboratory, offering a low-cost, low-power, and highly intuitive platform for decentralized diagnostics and disease surveillance in resource-limited settings.

The supporting videos provide real-time visualization of the NIR SPR signal shifts detected using the OUD integrated platform. All videos are time-lapsed to 20 s. Video 1: Details the DNA probe immobilization process on the SPR sensor. Video 2–6: Show the experimental procedures for different analyte concentrations (blank, 5 nM, 10 nM, 15 nM, 20 nM). Video 7–8: Show the experimental procedure for control samples and mimic samples spiked with the target analyte. Fig. S1. Photograph of the fully assembled portable OUD-based NIR-SPR system on a digital balance (total mass = 650 g). Fig. S2. Optimization of probe immobilization and functional response using a commercial Biacore SPR system. (a) Immobilization sensorgrams of biotinylated DNA probes co-injected with free biotin at ratios of 1:0, 1:0.25, and 1:0.5 on streptavidin-immobilized chips. (b) Functional detection of RNA targets followed by S9.6 antibody amplification under the same probe-density conditions. Fig. S3. (a) Long-term stability of OUD upconversion luminance (L/L_0) under continuous 5.0 V operation at (i) RT, 50 % RH, 1.0 mW cm^{-2}; (ii) RT, 50 % RH, 10.0 mW cm^{-2}; and (iii) 70 °C, 50 % RH, 1.0 mW cm^{-2}. (b) Fringe images before and after 30-h continuous operation under actual sensing conditions (0.29 mW cm^{-2}), showing negligible change in fringe visibility. (c) Fringe visibility under attenuated luminance using ND filters to simulate OUD degradation. The bright-green fringe remains clearly visible up to 0.6 OD (25 % transmittance) and discernible at 1.0 OD (10 % transmittance), demonstrating high tolerance to device degradation. Fig. S4. Triplicate SPR sensorgrams for each of six glycerol–water concentrations. Fig. S5. Upconversion-display images of blank pig serum at 10-fold (top panel) and 20-fold (bottom panel) dilutions under standard washing conditions. Each row represents one of three replicates; columns show (left) before target injection, (middle) before washing, and (right) after washing. Fig. S6. Specificity of the OUD-SPR assay in diluted pig serum. Upper panel: Sample (1) Non-target miRNA pool; lower panel: Sample (2) ASF-miRNAs + non-target miRNA pool. Fig. S7. Quantitative qPCR analysis of ASF-associated miRNAs in 20-fold diluted pig serum under four conditions: blank serum, non-target miRNA pool, and ASF-specific miRNAs at 0.5 nM and 40 nM together with the non-target miRNA pool. (a)

Table 1
Comparison of several recently developed naked-eye miRNA detection methods.

Method	Target	Detected by Naked-eye	Scheme	Assay time	Portability	Operational Complexity	Ref
Colorimetric detection	Cancer-associated miRNA	10 pM	SDA CRISPR/Cas12a Nanozyme	1.5 h	+	High	[39]
Colorimetric detection	Cancer-associated miRNA	2 pM	CHA Hydrogel Microchannel	1.5 h	+	High	[40]
Colorimetric detection	Cancer-associated miRNA	1 pM	RCA	3 h	+	High	[41]
Fluorescence	Cancer-associated miRNA	0.5 nM	DNA Walker	1.5 h	+	High	[42]
Smartphone-based SPR	Protein	Sub ug/mL – sub ng/mL	Affinity binding	15 min	++	Low	[7,11,12]
This Work	ASF-associated miRNA	5 nM	Affinity binding	10 min	++	Low	

Amplification curves for miR-199a-5p (left) and miR-122 (right). (b) Corresponding Cq values for the four sample conditions. Data are mean ± SD of three repeated experiments. Supplementary data to this article can be found online at https://doi.org/10.1016/j.cej.2025.170464.

CRediT authorship contribution statement

Li-Chen Su: Writing – original draft, Methodology, Conceptualization. **Xin-Hui Wang:** Writing – original draft, Investigation. **Chun-Jen Shih:** Writing – original draft, Investigation. **Zhi-Hao Huang:** Investigation. **Ying-Feng Chang:** Formal analysis. **Chen-Kai Chang:** Visualization. **Chi-Yun Wang:** Supervision. **Yu-Ching Huang:** Writing – review & editing, Methodology, Conceptualization. **Shun-Wei Liu:** Resources, Methodology, Conceptualization.

Declaration of competing interest

The authors declare the following financial interests/personal relationships which may be considered as potential competing interests: Li-Chen Su has patent pending to Ming Chi University of Technology. Yu-Ching Huang has patent pending to Ming Chi University of Technology. Shun-Wei Liu has patent pending to Ming Chi University of Technology. If there are other authors, they declare that they have no known competing financial interests or personal relationships that could have appeared to influence the work reported in this paper.

Acknowledgments

The authors gratefully acknowledge the financial support from the National Science and Technology Council (Grant Nos. NSTC-113-2221-E-131-021-MY3, NSTC-112-2221-E-131-021, NSTC-112-2622-E-131-006, NSTC-112-2628-E-131-001-MY4, NSTC-113-2221-E-131-009). Additionally, the corresponding author (S.-W. Liu) extends sincere thanks to Mr. Hsueh-Hsien Wu of Syskey Technology Co., Ltd. (Taiwan) for his invaluable assistance in designing the fabrication chambers. The authors gratefully acknowledge Dr. Sheng-Wei Lin of Technology Commons, College of Life Science, National Taiwan University, Taiwan who provided us with a lot of helpful information and assistance about Biacore T200™.

Data availability

Data will be made available on request.

References

[1] T.Y. Chen, J.L. Xin, S.J. Chang, C.J. Chen, J.T. Liu, Adv. Mater. Interfaces 10 (2023) 220220.
[2] J. Homola, S.S. Yee, G. Gauglitz, Sens Actuator B-Chem 54 (1999) 3–15.
[3] J. Zhou, Y. Wang, G.J. Zhang, Coord. Chem. Rev. 520 (2024) 216149.
[4] J.F. Masson, Analyst 145 (2020) 3776–3800.
[5] L.C. Chen, M.C. Li, K.R. Chen, Y.J. Cheng, X.Y. Wu, S.A. Chen, et al., Anal. Chem. 95 (2023) 7186–7194.
[6] Y.C. Huang, S.F. Wang, B.C. Chen, Z.S. Yang, M.C. Li, X.Y. Wu, et al., Sens Actuator B-Chem 400 (2024) 134898.
[7] C. Xiao, G. Ross, M.W.F. Nielen, J. Eriksson, G.I. Salentijn, W.C. Mak, Talanta 257 (2023) 124366.
[8] X. Zhang, Z. Li, W. Yan, A. Li, F. Zhang, X. Li, et al., Talanta 269 (2024) 125440.
[9] G.P. Singh, N. Sardana, Plasmonics 17 (2022) 1869–1888.
[10] H. Guner, E. Ozgur, G. Kokturk, M. Celik, E. Esen, A.E. Topal, et al., Sens Actuator B-Chem 239 (2017) 571–577.
[11] C. Xiao, J. Eriksson, A. Suska, D. Filippini, W.C. Mak, Anal. Chim. Acta 1201 (2022) 339606.
[12] Q. Zhang, Y. Li, Q. Hu, R. Xie, W. Zhou, X. Liu, et al., Lab Chip 22 (2022) 4941–4949.
[13] B.P. Nelson, A.G. Frutos, J.M. Brockman, R.M. Corn, Anal. Chem. 71 (1999) 3928–3934.
[14] A. Shalabney, I. Abdulhalim, Laser Photon Rev 5 (2011) 571–606.
[15] S.J. Chen, C.Y. Lin, Opt. Commun. 435 (2019) 102–107.
[16] H. Koresawa, K. Seki, K. Nishimoto, E. Hase, Y. Tokizane, T.A. Yano, et al., Sci. Rep. 13 (2023) 15655.
[17] D. Lakayan, J. Tuppurainen, M. Albers, M.J. van Lint, D.J. van Iperen, J.J.A. Weda, et al., Sens Actuator B-Chem 259 (2018) 972–979.
[18] P. Ghassemi, B. Wang, J. Wang, Q. Wang, Y. Chen, T. Joshua Pfefer, I.E.E.E. Trans. Biomed. Eng. 64 (2017) 1650–1653.
[19] S.W. Liu, C.C. Lee, C.H. Yuan, W.C. Su, S.Y. Lin, W.C. Chang, et al., Adv. Mater. 27 (2015) 1217–1222.
[20] Y. Hu, K. Wang, L. Chen, N. Li, Y. Lei, Innov Mater 2 (2024) 100067.
[21] C.J. Shih, Y.Z. Li, M.Z. Li, S. Biring, B.C. Huang, C.W. Liu, et al., Nano Energy 86 (2021) 106043.
[22] D.Y. Kim, T.H. Lai, J.W. Lee, J.R. Manders, F. So, Sci. Rep. 4 (2014) 5946.
[23] X. Hu, G. Xiao, Y.W. Li, S.E. Wu, Q. Chen, N. Li, et al., ACS Appl. Electron. Mater. 5 (2023) 5378–5385.
[24] C.J. Shih, C.Y. Lin, K. Chen, N.R. Al Amin, D. Luo, I.S. Hsu, et al., Adv. Sci. 10 (2023) 2302631.
[25] C.J. Shih, Y.C. Huang, T.Y. Wang, C.W. Yu, I.S. Hsu, A.K. Akbar, et al., Sci. Adv. 9 (2023) eadd7526.
[26] Y.C. Huang, T.Y. Wang, Z.H. Huang, S. Santiago, ACS Appl. Mater. Interfaces 16 (2024) 27576–27586.
[27] Z.B. Pang, S.Y. Chen, S. Cui, W.Z. Zhai, Y. Huang, X.T. Gao, et al., Animals 13 (2023) 1246.
[28] L.E.M. Dunn, A. Ivens, C.L. Netherton, D.A.G. Chapman, P.M. Beard, J. Virol. 94 (2020) e01515-01520.
[29] R. Chi, P.Y. Lin, Y.S. Jhuo, F.Y. Cheng, J.A.A. Ho, Talanta 267 (2024) 125159.
[30] F. Núñez-Hernández, L.J. Pérez, M. Muñoz, G. Vera, F. Accensi, A. Sánchez, et al., Virol. J. 14 (2017) 198.
[31] H. Šípová, S. Zhang, A.M. Dudley, D. Galas, K. Wang, J. Homola, Anal. Chem. 82 (2010) 10110–10115.
[32] C.Y. Lin, W.H. Wang, M.C. Li, Y.T. Lin, Z.S. Yang, A.N. Urbina, et al., Bioeng Transl Med 8 (2023) e10410.
[33] G.A. Müller, A. Lechner, M.H. Tschöp, T.D. Müller, Biomedicines 9 (2021) 277.
[34] J. Slaby, J. Homola, Biosens. Bioelectron. 212 (2022) 114426.
[35] X.H. Lu, C. Hu, D.L. Jia, W.J. Fan, W. Ren, C.H. Liu, Nano Lett. 21 (2021) 6718–6724.
[36] C. Bou-Nader, A. Bothra, D.N. Garboczi, S.H. Leppla, J.W. Zhang, Nat. Commun. 13 (2022) 1641.
[37] T. Wu, R. Lyu, C. He, Sci. Adv. 8 (2022) eabq2166.
[38] M.Y. Chen, Y.L. Yao, Y.L. Yang, M. Zhu, Y.J. Tang, S.Y. Liu, et al., Front. Genet. 10 (2019) 756.
[39] B. Luo, J. Zhou, X. Zhan, B. Ying, F. Lan, Y. Wu, Talanta 277 (2024) 126310.
[40] C.Y. Lee, J.Y. Jeong, H.J. Nam, C.A. Hong, ACS Appl. Mater. Interfaces 17 (2025) 5813–5822.
[41] H. Zhang, Y. Tang, Y. Zhou, Y. Wang, H. Si, L. Li, et al., Chem. Sci. 15 (2024) 9345–9352.
[42] Y. Wang, J.e. Qi, D. Ding, R. Deng, F. Jin, J. Ren, et al., Talanta 286 (2025) 127440.